Mechanical Systems and Signal Processing 91 (2017) 215–232

Contents lists available at ScienceDirect

Mechanical Systems and Signal Processing

journal homepage: www.elsevier.com/locate/ymssp

Analytical and experimental characterization of nonlinear coned disk springs with focus on edge friction contribution to force-deflection hysteresis

Nicholas P. Mastricola, Jason T. Dreyer, Rajendra Singh *

Acoustics and Dynamics Laboratory, Department of Mechanical and Aerospace Engineering, The Ohio State University, Columbus, OH 43210, USA

ARTICLE INFO

Article history:
Received 10 March 2016
Received in revised form 6 December 2016
Accepted 11 January 2017

Keywords:
Vibration isolators
Preload device
Experimental methods
Friction interfaces
Analytical models

ABSTRACT

Even though coned disk springs are widely used given their highly customizable design features, the literature on both analytical and experimental characterizations is sparse. This article overcomes the void by focusing on midrange displacements for a commercially available coned disk springs with square edges. A refined single disk spring model, capable of having asymmetric friction conditions imposed on the disk spring edges, is developed to predict the load-deflection and quasi-static hysteresis characteristics while relaxing prior limiting assumptions. A new quasi-static experiment is then proposed to measure the nonlinear load-deflection characteristics under four principal interfacial edge configurations — two symmetric and two asymmetric. In particular, the asymmetric friction conditions afford the opportunity to assess the validity of the long standing theory concerning the assumed location of the disk spring cross section rotation point. The imposition of asymmetric friction conditions on the disk spring also allows for the direct quantification of the contribution of asymmetric friction conditions on the disk spring contact edges. New analytical and experimental studies show that there are significant edge friction contributions to the hysteresis exhibited by the disk spring. Finally, stiffness parameters from both theory and experiment are briefly evaluated over midrange displacements.

1. Introduction

Coned disk springs, sometimes known as Belleville washers, belong to a family of diaphragm springs which assume several forms, such as wave washers and finger springs [1–4]. Coned disk springs are highly customizable for the desired application because of their unique stiffness and damping properties. The most common application for which disk springs are used is the application of preload; however, it has recently become apparent that it may be possible to leverage the disk spring's natural quasi-zero stiffness regime for the purpose of vibration isolation [1,2,5–8]. Overall, the literature concerning disk springs is relatively limited despite their utilization for over a century [3,4,9–26]. In particular, the experimental data from disk springs is sparse and most prior experimental studies mirror the simplifications used in analyses on which they are based. Therefore, the primary goals of this article are to develop a refined load-deflection model, propose a new disk spring experiment which is independent of preconceived analytical assumptions, and determine the nonlinear load-deflection relationships. The scope of this article is limited to commercially available coned disk springs with square edges as shown

* Corresponding author.
E-mail address: singh.3@osu.edu (R. Singh).

http://dx.doi.org/10.1016/j.ymssp.2017.01.009
0888-3270/

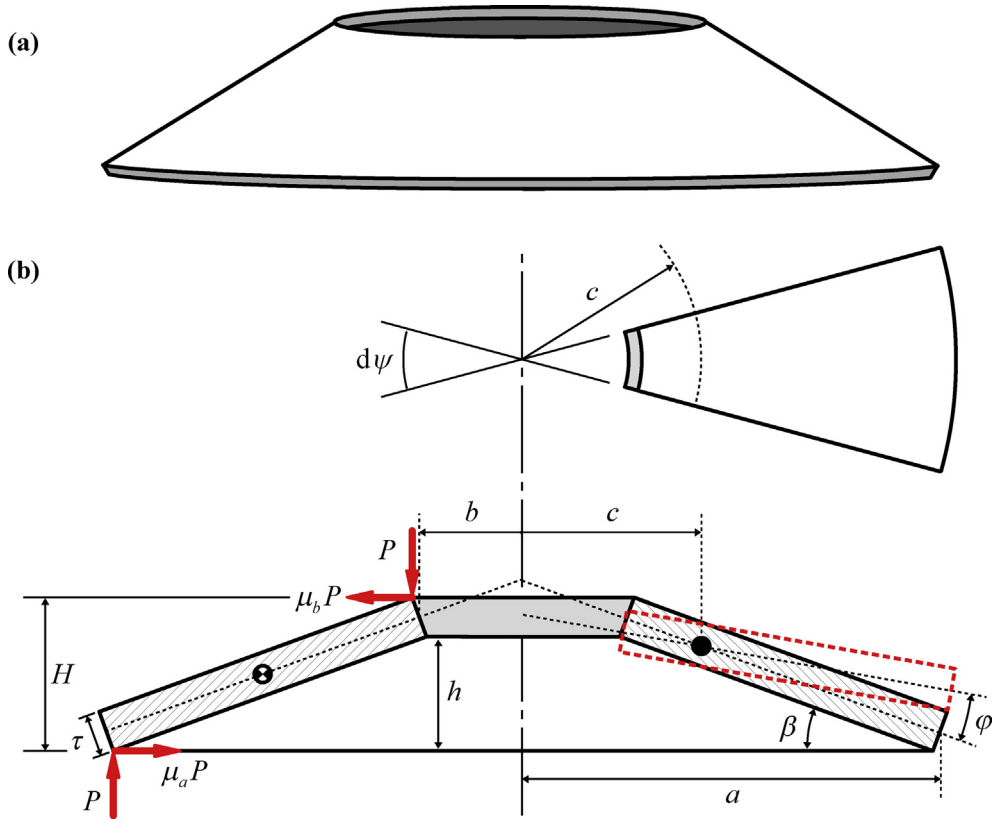

Fig. 1. Example case. (a) Coned disk spring with square edges; (b) top and cross section views of a coned disk spring with geometric parameters and loads: - - - cross section deformed position, ⟶ edge contact force. Symbols are defined in the text and in Appendix A.

in Fig. 1a; however, the methodology could be extended to diaphragm spring in general within the specified displacement range. The displacement range of interest is restricted to the midrange of their typical working displacements such that the resulting load-deflection results may be examined without influence from either initial nonlinearity due to asymmetry in the system or the characteristic stopper effect seen in load-deflection results.

2. Literature review

A method of analytically finding the load-deflection relationship was first proposed by Timoshenko as a textbook example [22] and his assumptions have permeated most of the subsequent disk spring analysis and experimentation. For instance, the following assumptions are still employed today: (a) the cross section's angular displacement is small; (b) there is no distortion of the cross section as it rotates about its neutral point during the loading process; (c) the forces at the disk spring boundaries are evenly and concentrically distributed; and (d) the radial stresses are negligible [9,21,22]. Almen and Laszlo, in their seminal paper of 1934 [9], expanded and generalized Timoshenko's example by including key aspects of disk spring kinematics which had been previously neglected; it remains the current *de facto* technical standard [9,18]. Major consequences of these assumptions are that the disk spring remains conical throughout the deformation process, and the boundary conditions at the upper and lower edges would not be satisfied [23]. Curti and Orlando [10] treated the coned disk spring as an annular plate, and linked the radial and tangential stresses by an equilibrium equation. Since Almen and Laszlo [9] erroneously neglected radial strain instead of radial stress, Curti *et al.* [13] correctly applied this assumption thereby allowing the natural conic geometry of the disk spring to be maintained. The formulation presented in Curti *et al.* [13] results in a load-deflection relationship that differs by a factor of $(1-\nu^2)$, where ν is the Poisson's ratio, from the denominator from the original Almen-Laszlo result.

Although Almen and Laszlo [9] pointed out that the friction forces within a disk spring stack could be varied via the stacking configuration, the presence of friction during the loading process has been largely neglected in most modeling efforts. Curti and Montanini [17] expanded the relationship presented in Curti *et al.* [13] by the addition of a Coulomb friction term to account for the friction forces at the outer and inner contacting edges of a single disk spring; it is predicated on the theoretical imprecision that the cross section rotates about its geometric center. This assumption implies that the outer and inner contact edges would translate the same distance in opposite directions during the loading process, and is of no real

consequence as long as both contact edges have the same Coulomb friction coefficient and no velocity dependent friction is present.

Prior experiments fall into four categories: classical load-deflection (half-load-cycle) testing, fatigue testing, hysteretic load-deflection (full-load-cycle) testing, and dynamic testing [9–13,15–19,24–26]. Classical experiments (half-load-cycle, load phase) only using a hydraulic actuator have been reported by several researchers [9–13] as a means to validating analytical derivations. Muhr and Niepage [15] experimentally investigated edge modification methods for friction reduction between a series disk spring stack and its mating surfaces. Subsequently Niepage [16] studied parallel disk spring stacks with conical platens using similar methods. Curti *et al.* [18,19] proposed an experimental test setup by which edge coefficients of friction of disk springs were found as model parameters. The resulting disk spring model was validated via full-load-cycle (load and unload) test [18].

3. Problem formulation

Since prior experiments [9,15,18,19] have been designed only to verify the physics assumed in analytical formulations, experimental characterization has been artificially limited. In order to counteract the predisposition to the prior assumptions, it is necessary to develop a new experiment that would allow the testing certain physics of the disk springs such as that the design process is not influenced by the analytical methods used. Hence, the specific objectives of this article are to: (1) propose a refined analytical load-deflection formulation for a single disk spring which accounts for different coefficients of frictions at the outer and inner edge contacts of the disk spring; (2) design a new well-controlled quasi-static characterization experiment capable of independent modification of the surfaces in contact with the disk spring; (3) assess the validity of prior theory made concerning the location of the disk spring cross section rotation point; and (4) quantify the contribution of asymmetric friction conditions on the inner and outer contact edges of the disk spring. The limitations of the aforementioned literature will be compared to the methods presented herein. Major assumptions made throughout this analytical and experimental work include the following (with reference to Fig. 1): (a) the loads are evenly distributed about the outer and inner contact edges; (b) angular deflections are sufficiently small such that small angle approximations may be utilized; (c) radial stresses within a disk spring are negligible; and (d) disk springs deform in an annularly symmetric process, in which the disk spring cross section rotates about its neutral point without distortion.

The coefficients of friction μ_a and μ_b at the outer and inner contact edges, respectively, as shown in Fig. 1b, are not required to be equal. By allowing the coefficients of friction at the outer and inner contact edges to be independent, the need arises to allow the natural geometry of the disk spring to assert itself. This is accomplished by not imposing any artificial restrictions on disk spring kinematics, and thereby allowing the cross section rotation point to be in its natural position rather than the center of the cross section. In the case of $\mu_a = \mu_b = \mu$, the friction forces would be equal and opposite at their respective edges, and therefore, the total moment due to the friction forces does not explicitly depend on the location of the rotation point of the cross section. However, the total moment due to the friction contribution explicitly depends on the location of the rotation point since the outer and inner edge friction forces will contribute in an unequal manner due to the length of their respective moment arms. Therefore, it is necessary to both analytically and experimentally explore the four principal friction conditions, as listed in Table 1.

4. Development of a refined analytical model for a single disk spring

The load-deflection relationship is derived from three infinitesimal moments (M) which act on the radial cross section (Fig. 1b) of a single disk spring [9,18]. The equilibrium equation that must be satisfied (when friction is neglected) is $dM_P = dM_{R1} + dM_{R2}$, where dM_P is the external moment due to the applied load, dM_{R1} is the reaction moment due to the radial displacement, and dM_{R2} is the reaction moment due to the change in curvature. The external moment dM_P may be expressed below in terms of the load P (distributed about the loading edges), the mid-surface outer radius a, the mid-surface inner radius b, the shell thickness τ, the cone base angle β, the relative rotational displacement of the cross section φ (where $0 \leqslant \varphi \leqslant \beta$), and the sector angle ψ, as shown in Fig. 1b.

$$dM_P = \frac{P}{2\pi}[(a-b) - \tau\sin(\beta-\varphi)] \cdot d\psi \approx \frac{P}{2\pi}(a-b) \cdot d\psi \tag{1}$$

Table 1
Four principal friction conditions that are experimentally and analytically evaluated.

Principal friction condition	Outer edge friction coefficient μ_a	Inner edge friction coefficient μ_b
Φ_1	High	High
Φ_2	Low	Low
Φ_3	High	Low
Φ_4	Low	High

For most commercially available disk springs, $\tau \sin(\beta - \varphi)$ will be approximately two orders of magnitude smaller than $(a - b)$, and therefore, may be considered negligible. Likewise, the expressions for dM_{R1} and dM_{R2} may be written as

$$dM_{R1} = E\tau\varphi(\beta - \varphi)\left(\beta - \frac{\varphi}{2}\right)\left[\frac{a^2 - b^2}{2} - \frac{(a-b)^2}{\ln\alpha}\right] \cdot d\psi \tag{2}$$

and

$$dM_{R2} = \frac{E\tau^3\varphi}{12} \ln\alpha \cdot d\psi \tag{3}$$

where α is the ratio a/b and E is the Young's modulus. Substituting the differential moments into the equilibrium condition yields the load-deflection relationship for a single frictionless disk spring as a function of the relative rotational displacement φ, and is written as

$$P_{L1}(\varphi) = \left(\frac{E\pi\varphi}{a-b}\right)\left\{(\beta - \varphi)\left(\beta - \frac{\varphi}{2}\right)\left[a^2 - b^2 - \frac{2(a-b)^2}{\ln\alpha}\right]\tau + \frac{\tau^3}{6}\ln\alpha\right\} \tag{4}$$

The more common form of Eq. (4) is reached by applying the substitutions $\beta \approx h/(a-b)$ and $\varphi \approx \delta/(a-b)$, where δ is axial spring deflection. It should be noted that the expressions for β and φ are simplified by applying $\cos(\beta - \varphi) \approx 1$ and $\sin(\beta - \varphi) \approx \tan(\beta - \varphi) \approx \beta - \varphi$. These approximations may be substituted without sacrificing accuracy for the majority of cases since β is typically under 10° for most commercially available disk springs. Thus, the load-deflection relationship $P_{L3}(\delta)$, as derived in Curti *et al.* [13], is

$$P_{L3}(\delta) = \frac{E\delta\pi}{a^2}\left(\frac{\alpha}{\alpha-1}\right)^2\left[(h-\delta)\left(h - \frac{\delta}{2}\right)\left(\frac{\alpha+1}{\alpha-1} - \frac{2}{\ln\alpha}\right)\tau + \frac{\tau^3}{6}\ln\alpha\right]. \tag{5}$$

As shown previously by Curti and Montanini [18], the friction at the contact edges of a single disk spring can be accounted for by formulating an infinitesimal moment. By including the infinitesimal moment due to the imposition of a symmetric friction condition, Curti and Montanini [18] have also shown that the load-displacement relationship, with the inclusion of friction, may be expressed as

$$P_{L4}(\delta) = \frac{\frac{E\delta\pi}{a^2}\left(\frac{\alpha}{\alpha-1}\right)^2\left[(h-\delta)\left(h-\frac{\delta}{2}\right)\left(\frac{\alpha+1}{\alpha-1} - \frac{2}{\ln\alpha}\right)\tau + \frac{\tau^3}{6}\ln\alpha\right]}{1 \mp \mu_e \frac{h-\delta+\tau}{a-b}} = \frac{P_{L3}(\delta)}{1 \mp \mu_e \frac{h-\delta+\tau}{a-b}}, \tag{6}$$

where μ_e is the static coefficient of friction on each disk spring contact edge (*i.e.* $\mu_a = \mu_b = \mu_e$), and $P_{L4}(\delta)$ is the displacement dependent spring force determined by Curti and Montanini [18]. Eq. (6) makes the simplifying assumption that the friction conditions at the outer and inner edges are identical, which implies that the total friction force contributions at the outer and inner contact edges are equal and opposite (it should be noted that this is not a necessary condition to maintain static equilibrium). From the physical perspective, this condition is only possible through the imposition of an artificial geometric constraint $(a - c) = (c - b)$, which forces the disk spring cross section to rotate about its geometric center. While this artificial geometric constraint facilitates reasonable results for symmetric friction conditions, it cannot be regarded as true for the general case of an asymmetric friction condition where $\mu_a \neq \mu_b$.

The aforementioned analytical imprecision is rectified by removing the necessity that the coefficients of friction at the outer and inner contact edges, μ_a and μ_b respectively, must be equal. The removal of this physical restriction mandates that the actual value of c must be accounted for such that $(a - c) \neq (c - b)$, as shown in Fig. 1b, and thereby addressing the contact edges as unique friction entities. Hence, the total moment due to edge friction is

$$\begin{aligned} dM_{ef} &= \pm\tfrac{P}{2\pi}\left\{\left[a\mu_a - b\mu_b - c(\mu_a - \mu_b)\right]\tan(\beta - \varphi) + \tfrac{\tau}{2}(\mu_a + \mu_b)\cos(\beta - \varphi)\right\} \cdot d\psi \\ &= \pm\tfrac{P}{2\pi}\left\{\left[a\mu_a - b\mu_b - c(\mu_a - \mu_b)\right](\beta - \varphi) + \tfrac{\tau}{2}(\mu_a + \mu_b)\right\} \cdot d\psi, \end{aligned} \tag{7}$$

where P is the spring force. The infinitesimal moment due to the edge friction may now be added to the equilibrium condition of the radial cross section as shown in Eq. (8).

$$dM_P = dM_{R1} + dM_{R2} + dM_{ef} \tag{8}$$

Similar to that of Eq. (4), the single disk spring load-deflection relationship, inclusive of edge friction, takes the form

$$P_f(\varphi) = \frac{\left(\frac{E\pi\varphi}{a-b}\right)\left\{(\beta - \varphi)(\beta - \frac{\varphi}{2})\left[a^2 - b^2 - \frac{2(a-b)^2}{\ln\alpha}\right]\tau + \frac{\tau^3}{6}\ln\alpha\right\}}{1 \mp \left\{\frac{\left[a\mu_a - b\mu_b - c(\mu_a - \mu_b)\right](\beta-\varphi)}{(a-b)} + \frac{\tau(\mu_a+\mu_b)}{2(a-b)}\right\}}. \tag{9}$$

Applying the aforementioned substitutions and simplifications to Eq. (9) results in the final form of the load-deflection relationship given by

$$P_f(\delta) = \frac{\frac{E\delta\pi}{a^2}\left(\frac{\alpha}{\alpha-1}\right)^2\left[(h-\delta)\left(h-\frac{\delta}{2}\right)\left(\frac{\alpha+1}{\alpha-1}-\frac{2}{\ln\alpha}\right)\tau+\frac{\tau^3}{6}\ln\alpha\right]}{1\mp\left\{\frac{\left[a\mu_a-b\mu_b-c(\mu_a-\mu_b)\right](h-\delta)}{(a-b)^2}+\frac{\tau(\mu_a+\mu_b)}{2(a-b)}\right\}} = \frac{P_{L3}(\delta)}{1\mp\left\{\frac{\left[a\mu_a-b\mu_b-c(\mu_a-\mu_b)\right](h-\delta)}{(a-b)^2}+\frac{\tau(\mu_a+\mu_b)}{2(a-b)}\right\}}. \tag{10}$$

Eq. (10) indeed reduces to Eq. (6) when $\mu_a = \mu_b$. Therefore, the prior formulation by Curti and Montanini [18] may be regarded as a special case of Eq. (10) for disk springs having similar friction conditions on each of its contacting edges. The explicit dependence of Eq. (10) on c can be leveraged to explore the sensitivity of this parameter on the force output of the disk spring, as well as assertions as to the deformation mechanisms during the loading process. Two different definitions of c exist in literature due to the varying assumptions that have been made in various formulations. The older formulation, as shown in Eq. (11) from Almen and Laszlo [9], is often used, albeit based on incorrect assumptions.

$$c_{L1} = \frac{a-b}{\ln\alpha} \tag{11}$$

Conversely, the lesser known formulation for c,

$$c_{L2} = a\left(\frac{v}{1-v}\right)\left(\frac{\alpha^{(v-1)}-1}{1-\alpha^v}\right), \tag{12}$$

was presented by Curti and Orlando [10] more recently under modified assumptions.

5. Typical disk spring load-deflection and hysteresis characteristics under four friction conditions

The disk springs, and its associated parameters, used throughout this work are either given by the supplier, calculated from the supplier provided values, or measured directly from the supplier provided CAD file. The common disk spring parameters are shown in Table 2.

The load-deflection results shown in Figs. 2a and 2b are found using Eq. (10) with $c = c_{L1}$, where $c_{L1}/a = 1.226$. Correspondingly, using $c = c_{L2}$ in Eq. (10), where $c_{L2}/a = 1.231$, yields the results shown in Figs. 2c and 2d. The metric c/a is bounded such that $[1 \quad \alpha]$, where $\alpha = 1.525$ for the case at hand. Each of the four friction conditions (as listed in Table 1) are as follows: symmetric high friction (Φ_1 where $\mu_a = \mu_b = 0.5$ for the numerical example); symmetric low friction (Φ_2 where $\mu_a = \mu_b = 0.3$ for the numerical example); the first asymmetric friction condition with the increased friction on the outer edge (Φ_3 where $\mu_a = 0.5$ and $\mu_b = 0.3$ for the numerical example); and the second asymmetric friction condition with the higher friction coefficient on the inner edge of the disk spring (Φ_4 where $\mu_a = 0.3$ and $\mu_b = 0.5$ for the numerical example) are represented by the solid dark, solid light, dashed dark, and dashed light lines, respectively.

In each of the cases shown in Figs. 2a and 2c, there is no change in the overall shapes of the hysteresis loops. As expected, the largest and smallest hysteresis loops are found using Φ_1 and Φ_2, respectively, which would have been the same result using Eq. (6). The hysteresis loops of Φ_3 and Φ_4 split the difference between the loops of the bounding cases — this is an intuitive result given the geometry of the disk spring (Fig. 1b). However, the hysteresis loops of Φ_3 and Φ_4 exhibit an almost imperceptible difference between each other, as observed in Figs. 2a and 2c, regardless of the value of c chosen. Conversely, Φ_3 shows a distinctly larger hysteretic force difference than that of Φ_4 in both Figs. 2b and 2d. Comparing Φ_3 in Figs. 2b and 2d, it is seen that the hysteretic force difference of Φ_3 exhibits an increasing trend which is proportional to c/a, which suggests that the moment arm of the high friction outer edge is lengthening. It is also observed that the hysteretic force difference of Φ_4 has the opposite trend due to a reduction of the moment arm of the high friction inner edge.

6. Development of a new quasi-static experiment

Two primary experimental concerns, which are unique to disk springs, must be given special consideration during the design of a quasi-static experimental apparatus; they are: (1) the disk spring yields a high force with a relatively low corresponding displacement and (2) concentric alignment of all components must be ensured. The scale mismatch between

Table 2
Disk spring parameters and specifications.

Parameter or specification	Value or characteristic
Mid-surface outer radius, a	14.068 mm
Mid-surface inner radius, b	9.2238 mm
Cone height, h	0.6998 mm
Disk spring height, H	1.0998 mm
Cone base angle, β	0.1435 rad
Shell thickness, τ	0.4013 mm
Material	High-carbon spring steel
Typical use	25.4 mm ball bearing preload washer
Supplier	McMaster-Carr

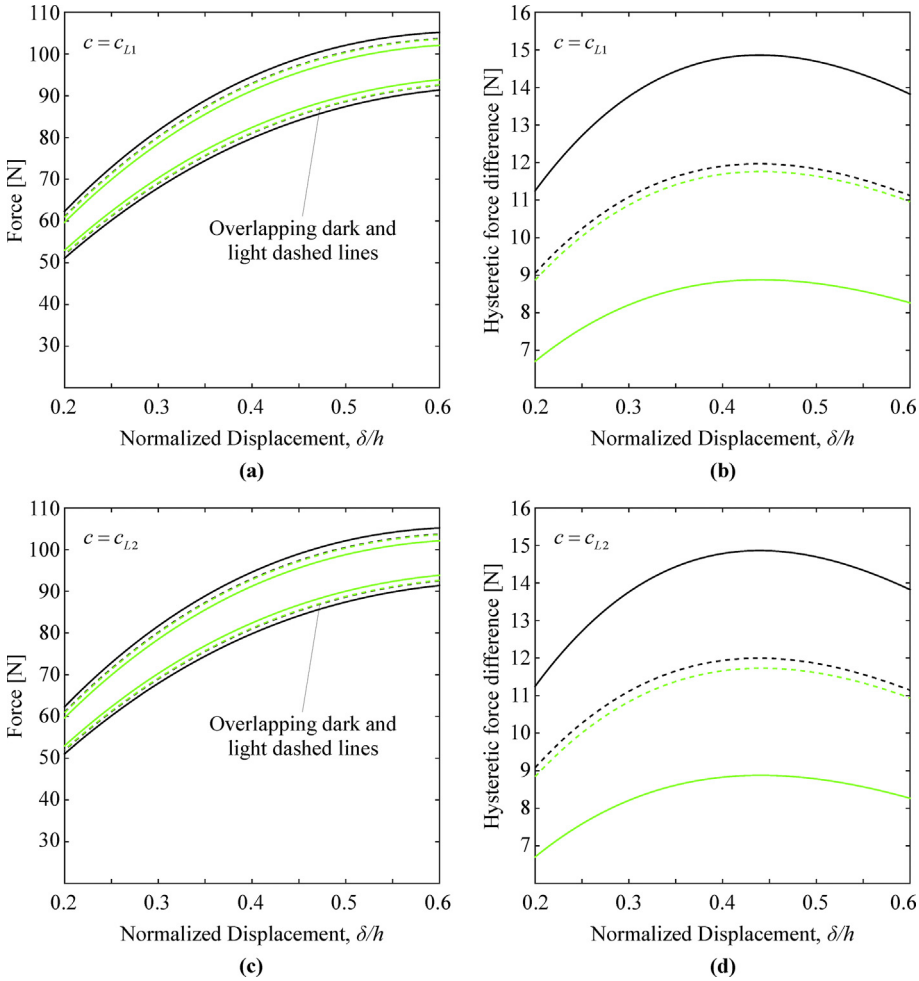

Fig. 2. Typical load-displacement results of refined model under four different friction conditions as listed in Table 1. (a) Load-displacement curves symmetric and asymmetric disk spring friction conditions with $c = c_{L1}$; (b) hysteretic force difference with $c = c_{L1}$; (c) load-displacement curves symmetric and asymmetric disk spring friction conditions with $c = c_{L2}$; and (d) hysteretic force difference with $c = c_{L2}$. Key: —— Φ_1, —— Φ_2, - - - - Φ_3, and - - - Φ_4.

the displacement input and force output of the disk spring creates several issues which will be dealt with through a combination of experimental process control, instrumentation selection, and level of control over the friction interface surfaces – the latter will be address in the following section. Commercial test frames with hydraulic actuation (*e.g.* MTS model 831.50 [27] and LINK model 1620 [28]) were initially considered for making the measurements required for this study. The MTS 831.50 is specifically designed for high frequency elastomer testing with higher loads and displacements, relative to the disk spring. The LINK 1620 is essentially a brake pad tester designed to measure very high loads at low displacements [28]. Measurements on disk springs, being a low displacement and low force elements compared to the usual specimens tested in such load frames, would require modification of the commercial test systems. Therefore, a custom test frame was chosen in favor of the aforementioned commercial test frames. Initially, a pneumatic cylinder was selected as an actuator since it would effectively make a force-controlled experiment, which would have allowed for the investigation of force-dependent phenomena (*e.g.* stick-slip). However, the inability to accurately and precisely control the air inlet and outlet pressures of the pneumatic cylinder led to inconsistency within the data and the eventual abandonment of pneumatic actuation in favor of a voltage controlled power screw. Concurrently, a string potentiometer was initially chosen for displacement measurement. Likewise, the string potentiometer was abandoned because of its relatively high noise floor and angle offset error due to a slight misalignment between the apparatus's line of action and the potentiometer's string. A high resolution linear variable differential transformer (LVDT) is then selected in place of the string potentiometer. The specifications of the selected LVDT [29], as well as the selected load cell [30], are shown in Table 3.

The main portion of the designed load-displacement test apparatus, shown in Fig. 3, consists of a variable speed power screw, a pair of parallel platens, replaceable friction surfaces affixed to the upper and lower platens, a high resolution LVDT, and a load cell. The lower platen's angular orientation relative to the upper platen, horizontal and transverse alignment relative to the upper platen, and axis of vertical motion are maintained by centering support assembly sipper-foot which

Table 3
Selected sensor specifications for proposed experiment [29,30].

	LVDT	Load cell
Manufacturer	Omega Engineering, Inc.	Omegadyne
Model	LD500-2.5	LCR-2k
Range	±2.5 mm	0–8896N

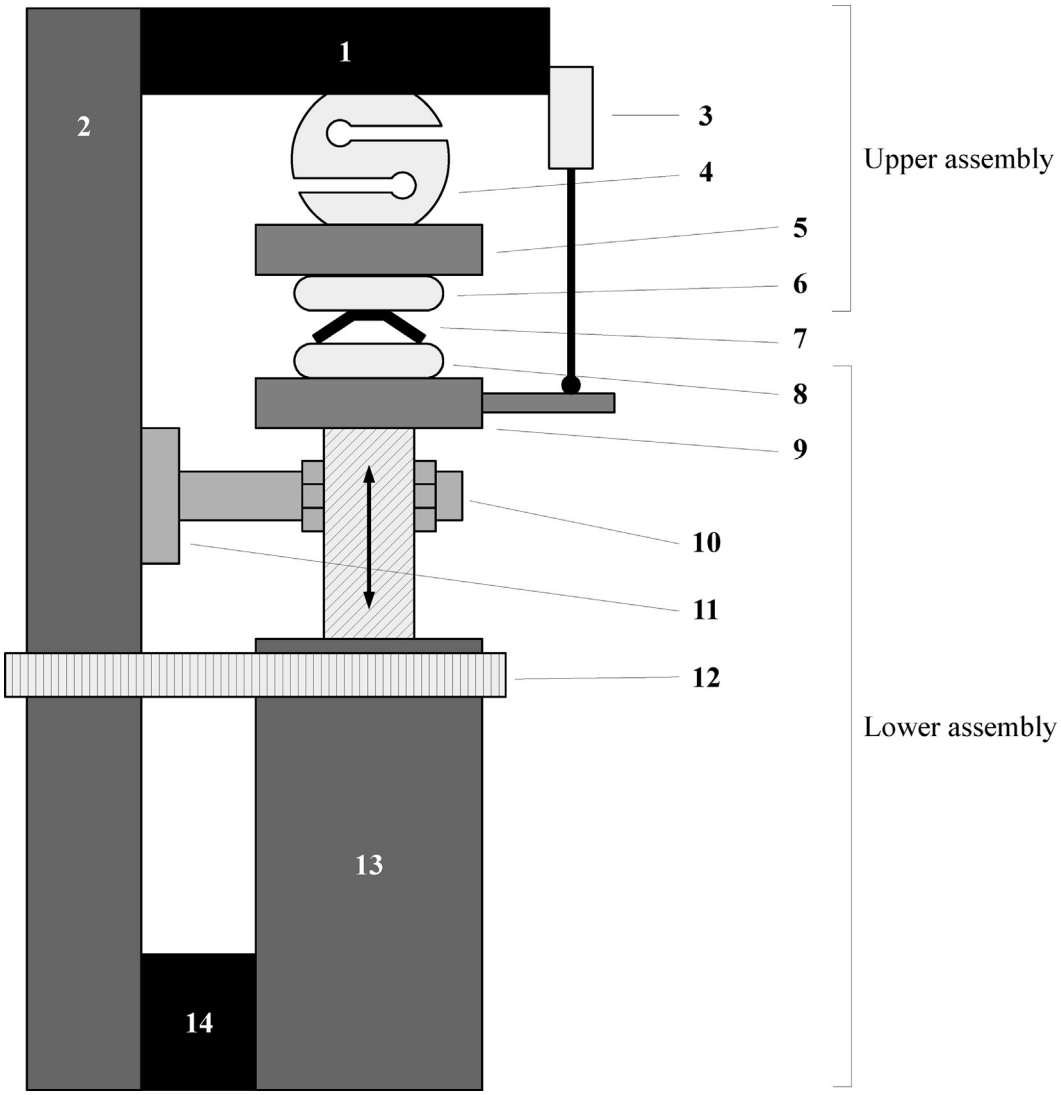

Fig. 3. New disk spring load-displacement test apparatus. Key of components: (1) rigid top support, (2) rigid back support, (3) high resolution LVDT, (4) force transducer, (5) upper platen, (6) upper friction surface, (7) disk spring, (8) lower friction surface, (9) lower platen, (10) centering support assembly, (11) slipper-foot, (12) tensioning band clamp, (13) voltage controlled power screw, and (14) rigid bottom support, where ◄► is the power screw line of action.

rides on the rigid back support. The slipper-foot is held in constant contact with the rigid back support by the tensioning band clamp. Annular shims are used as the substrate for the friction surfaces, and are attached to the platens such that both are in alignment with the load cell. The disk spring is aligned to the friction surfaces using a simple gauge block that is removed prior to beginning each test. The single screw attachment of the upper and lower assemblies, in combination with the centering and support guide, allows the platens to be brought into parallel and maintain the proper alignment.

The action required to lubricated surfaces does not allow for the independent control of the upper and lower friction surfaces; however, the use of well controlled unlubricated surfaces facilitates the ability to investigate both the symmetric and

Table 4
Interfacial friction conditions implemented in the new quasi-static experiment (Fig. 3).

Experimental surface conditions	Contact surface pair	
	Outer contact edge	Inner contact edge
Φ_{E1}	30 μm film	30 μm film
Φ_{E2}	0.3 μm film	0.3 μm film
Φ_{E3}	30 μm film	0.3 μm film
Φ_{E4}	0.3 μm film	30 μm film

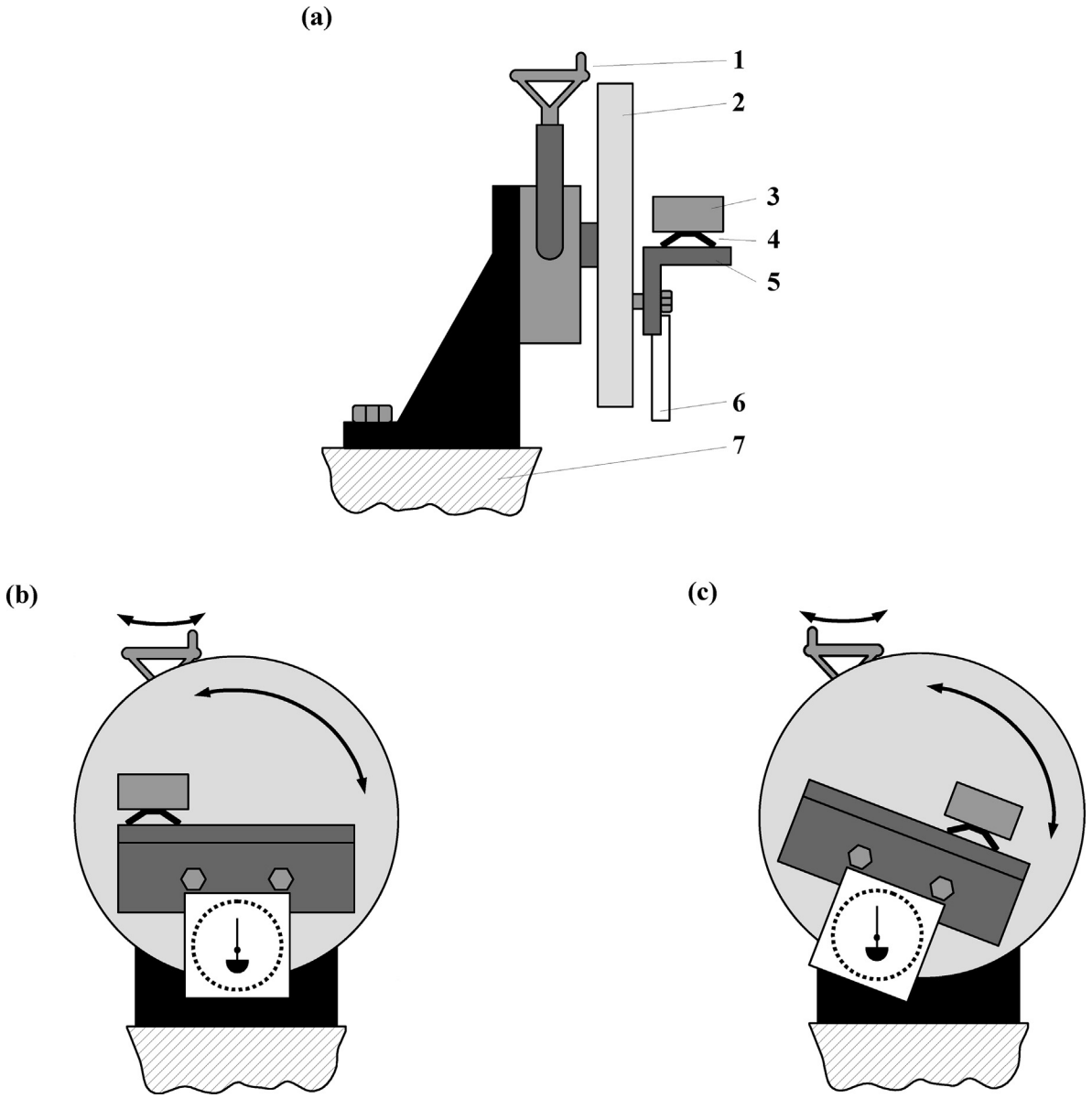

Fig. 4. Apparatus used to determine the static friction. (a) Side view in initial position, (b) front view in initial position, and (c) front view in final position, where ⌒ shows the out of plane rotary motion of the tilt adjustment and the resulting in plane motion of the rotary table. Key of components: (1) tilt adjustment, (2) rotary table, (3) mass glued to a (4) disk spring, (5) friction surface adhered to a trued angle iron, (6) weighted needle protractor, and (7) the base plate.

asymmetric friction cases outlined in the preceding section. Well controlled platen surfaces can be obtained by utilizing differing grades of lapping film — a commercially available product that is comprised of tightly graded aluminum oxide abrasive, which is commonly used in the fiber optics industry to polish custom connectors [31]. Due to the nature of the lapping films intended use, lapping film produce an incredibly consistent surface which is an ideal choice to induce well controlled friction boundary. The lapping film is positioned, affixed to the annular shims using a thin and even coat of cyanoacrylate adhesive over the entire shim surface, and allowed to cure completely under pressure. Table 4 shows the lapping film grit rating (30 μm for high friction and 0.3 μm for low friction) utilized in the experimental apparatus to produce the desired friction at the edges of the disk spring for the symmetric friction conditions (Φ_{E1} and Φ_{E2}), and the asymmetric friction conditions (Φ_{E3} and Φ_{E4}). Each of the experimental friction conditions are analogous to their analytical counterpart defined in the preceding section.

While the lapping film being used to control the interfacial friction conditions in the quasi-static experiment are made of tightly graded aluminum oxide such that the mean asperity height is known, it has never been characterized in regards to its associative static friction coefficient μ_s. Therefore, the quantification of the lapping film's friction properties is vital for both experimental and analytical efforts. The laws of static friction dictate that the static coefficient of friction is independent of both normal force and area of contact. If a block on an inclined plane is considered, it can be shown that the relationship between μ_s and the angle of repose θ_s is $\mu_s \approx \arctan\theta_s$ [32]. Therefore, it is necessary to construct an apparatus which is capable of varying and measuring the angle of an inclined plane in a consistent manner. As shown in Fig. 4, a milling machine rotary table is selected for the bases of this apparatus, to which a trued piece of angle iron was bolted. The lapping film is affixed to the angle iron using the method outlined in the previous subsection. Using the same adhesive, a disk spring is affixed to a small piece of steel. After both the disk spring and substrate are allowed to cure, the mass-disk spring block is placed at one end of the friction surface. The angle of the table is slowly varied until the mass began to slip; θ_s was then read off of the weighted protractor to the nearest quarter-degree.

Eight clockwise trials and eight counterclockwise trials are carried out for both the 0.3 μm and 30 μm lapping films. During the sixteen total trials (N), the angular orientation of the disk spring block relative to the friction interfaces was varied over four positions in order to mitigate any local confluences of variable that may skew the results. A visual summary of the computed μ_s for each of the measured θ_s is shown in Fig. 5, and the relevant statistics for each data set may be found in Table 5.

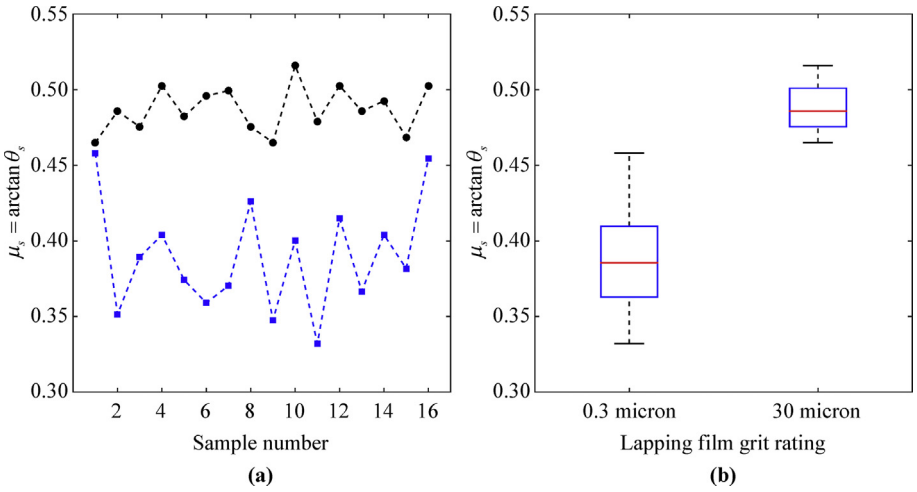

Fig. 5. Measured static friction values for 16 samples using the apparatus of Fig. 4. (a) μ_s determined from each measured θ_s, where ···●··· are 30 μm lapping film points and ···■··· are the 0.3 μm lapping film points. (b) Boxplot of experimentally determined μ_s for each lapping film grit.

Table 5
Experimentally determined μ_s statistics for each lapping film grit rating.

Parameter	Lapping film grit ratings	
	0.3 μm	30 μm
Number of samples, N	16	16
Mean, $\overline{\mu_s}$	0.3896	0.4871
Median	0.3855	0.4858
Standard deviation, s	3.662×10^{-2}	1.527×10^{-2}
Standard error, $SE_{\overline{\mu_s}}$	9.155×10^{-3}	7.817×10^{-3}
95% confidence interval	[0.3713 0.4080]	[0.4795 0.4948]

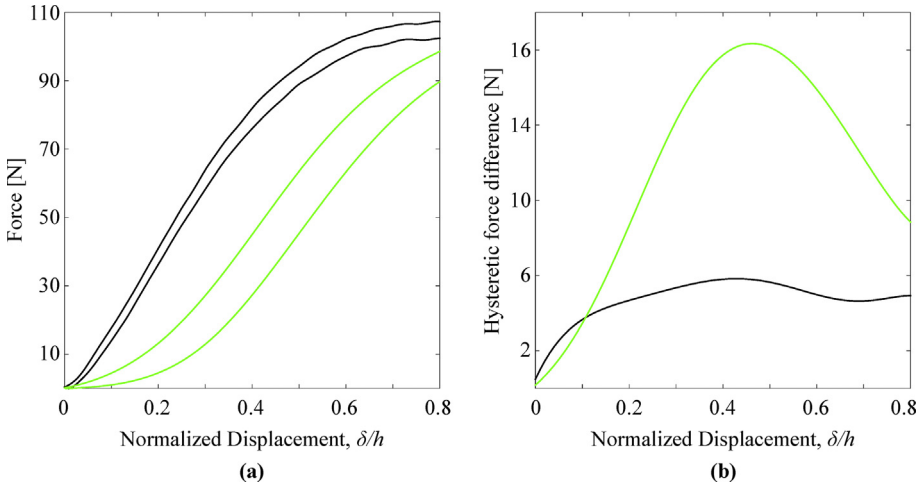

Fig. 6. Measurements at two loading rates of a single disk spring element using the quasi-static test apparatus (Fig. 3): (a) load-deflection curves and (b) corresponding hysteretic force magnitudes. Note that these measurements have been conducted under friction conditions with μ_s lower than the characterized 0.3 μm grit film. Key: —— 1 mm/s (quasi-static limit), —— 10 mm/s

It is evident when comparing each of the data sets that the 30 μm lapping film performed much more consistently during the tilt tests Fig. 5b, as well as in the respective standard deviation of each data set (Table 5). One may be predisposed to assume that this is the result of wear on the lapping film or a "filling" effect; however, this appears to not be the case since the data does not have a specific trend directionality (*i.e.* increasing or decreasing) in Fig. 5a. Therefore, the range exhibited by the 0.3 μm lapping film data set should be regarded as acceptable random variation in the measurements. Hence, it is reasonable to assume, for the purposes of this article, that the actual value for μ_s associated with either of the friction papers will fall within their respective 95% confidence intervals (mean-centered), also shown in Table 5.

The loading and unloading rates are set to the quasi-static velocity limit, which is a sufficiently slow rate such that the resulting quasi-static measurements are a reasonable representation of acquiring independent static measurements over the displacement range of interest. A loading and unloading rate of 1 mm/s is found to be the quasi-static velocity limit by increasing the loading and unloading rates until an increase hysteretic force is observed. This effect is observed in the load-deflection measurements (Fig. 6a), and corresponding hysteretic force differences (Fig. 6b) of a single disk spring element at loading rates of 1 mm/s (the quasi-static limit) and 10 mm/s. Comparing the two load-deflection characteristics (Fig. 6a) measured at their respective cycling rates, pronounced changes in both the overall shape of the characteristics as well as the hysteretic force difference (Fig. 6b) between the loading and unloading cycles are observed. The hysteretic force differences (Fig. 6b) show an appreciable difference in magnitude which flattens significantly with decreasing loading rate. This study presented herein has been restricted to only quasi-static measurements in order to have a scientific basis for comparison with prior work that has been done in the same regime. Furthermore, the changes between the load-deflection characteristics in Fig. 6 indicate that there is an appreciable contribution from a velocity dependent term which is not included in either the proposed or prior load-deflection relationships.

7. Validation of the new quasi-static experiment

A linear helical spring is used to validate the proposed test apparatus (Fig. 3) through stiffness comparison. The nominal stiffness, k_{HS}, is approximated to be 24 N/mm using the specifications shown in Table 6 with empirical relationship [33]

$$k_{HS} = \frac{d^4 G}{8D^3 \eta}. \tag{13}$$

By a separate static load-deflection test, k_{HS} is determined to be approximately 23 N/mm. The helical spring is deflected approximately 1 mm. Then, the load-deflection characteristic (shown in Fig. 6) of the helical spring is measured over the next 1 mm range of its total displacement. The low load range of the validation test is selected in order to makes sure that the selected load is suitable since its maximum capacity is much higher than needed (see Table 3). While the initial lengths of the validation spring and the selected disk springs are significantly different ($\ell_0 - H = 53.81$ mm), the high resolution LVDT can be translated along an axis parallel to the power screw's line of action which allows the datum of the displacement measurement to be set at any point in the power screw's range of motion. The total stroke length of the LVDT (Table 3) is, therefore, the limiting factor for the displacements measurement. The measured load-deflection characteristic data and lines of best fit for the helical spring of both the loading and unloading processes are shown in Fig. 7. The stiffness parameters of 24.4 N/mm for the loading process and 24.6 N/mm for the unloading process are determined though linear regression.

Table 6
Linear helical spring parameters and specifications.

Parameter or specification	Value or characteristic
Wire diameter, d	4.55 mm
Mean spring diameter, D	31.45 mm
Initial length, ℓ_0	54.91 mm
Number of coils, η	5.75
Material	High-carbon spring steel
Modulus of rigidity (typical[a]), G	80 GPa

[a] Typical value of G assumed from commonly reported values for AISI 1050 and AISI 1095 high carbon spring steels [34,35].

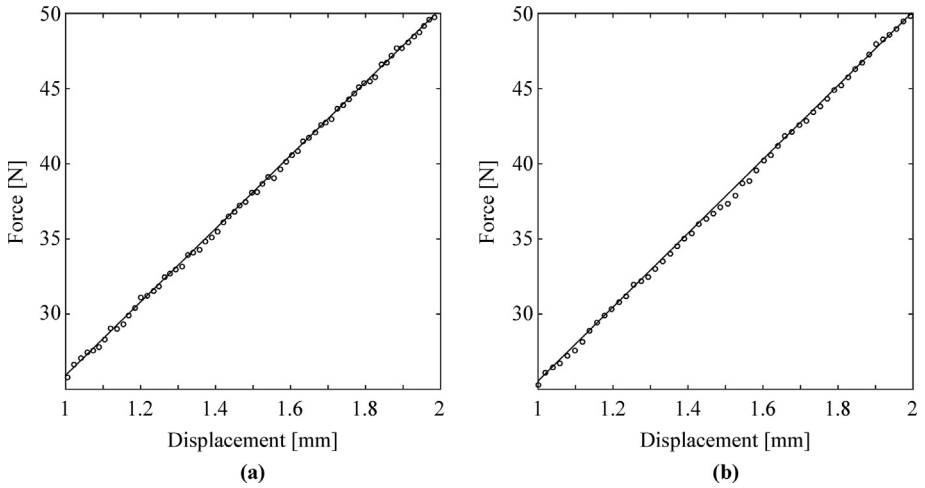

Fig. 7. Measured load-deflection characteristics of a linear helical spring. (a) Loading process data. (b) Unloading process data. Key: ○ representative measured data and —— line of best fit.

Table 7
Summary of analytically and experimentally determined spring rates k_{HS} for a linear helical spring.

Determination method	k_{HS}, N/mm	Percent difference
Analytical approximation	24.0	–
Static load-deflection experiment	23.0	4.26%
Quasi-static load-deflection experiment, loading process	24.4	1.65%
Quasi-static load-deflection experiment, loading process	24.6	2.47%

Table 7 shows a summary of the estimated helical spring rates from Eq. (13), the static load-deflection test, and both loading and unloading quasi-static tests. The percent differences have been calculated using the analytical approximation as the baseline value. It is interesting to note that both the loading and unload quasi-static determination methods are significantly closer to the analytical results than the static load-deflection test. Furthermore, the load cell resolution is acceptable, based on the validation measurement (Fig. 7) and stiffness comparisons (Table 7), for the disk spring load-deflection measurement. This small amount of hysteretic behavior (observed between the loading and unloading quasi-static tests) could be due to a combination of several different factors present in the test setup or in the helical spring itself. However, the hysteresis exhibited by disk springs under similar testing procedures is typically several orders of magnitude higher than seen in this validation experiment; therefore, the hysteresis which manifests in this validation experiment can be considered entirely negligible. Moreover, load-displacement characteristic of the test frame (shown in Fig. 8) is measured under the same loading conditions used for the validation and disk springs. The stiffness of the test frame is calculated, using the measurements shown in Fig. 8, to be 19.3 kN/mm, which is significantly higher than the disk spring stiffness over the displacement range of interest.

8. Comparison of measurements with predictions of refined model

The raw measured data for each trial, collected using the method outlined previously, is fitted to a fifth-order polynomial which maintains that characteristics of the collected measurements over the full displacement range of the disk spring (a

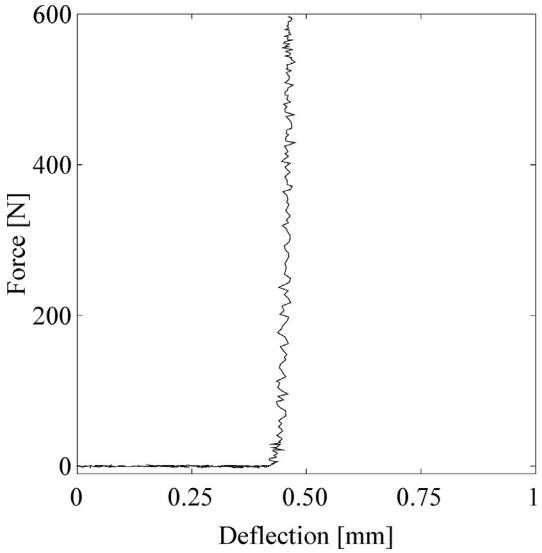

Fig. 8. Measured test frame (Fig. 3) load-deflection characteristic used to calculate the corresponding stiffness. Here, $k_{TF} = 19.3$ kN/mm.

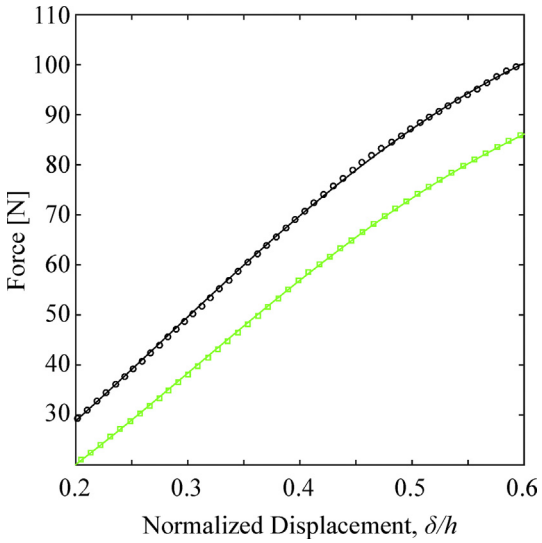

Fig. 9. Typical disk spring load-deflection measurements from the proposed experiment along with fifth-order polynomial fits. Key: ○ measured during loading process, —— loading process curve of best fit, □ measured during unloading process, and —— unloading process curve of best fit.

representative data set over the range of interest is shown in Fig. 9). The mean load displacement characteristic is found by averaging the best fit curves of the raw measurements (Fig. 10a). Fig. 10b shows the hysteretic force difference curves computed from the average load-displacement curves. The experimental load-displacement curves are similar to the overall shape of the hysteresis loop of the analytical predictions (Figs. 2a and 2c); however, the magnitudes of the experimental results differ significantly from the magnitudes of their analytical counterparts. Based on the hysteretic force difference curves of the symmetric friction conditions (Φ_{E1} and Φ_{E2} in Fig. 10b), it can be seen that the largest hysteretic difference is exhibited by the Φ_{E1}, which is consistent with the analytical results (Figs. 2b and 2d). The Φ_{E1} load-displacement relationship appears more linear at lower forces than the other experimental curves or accompanying theory, which contributes to the overall lower forces produced by a disk spring with Φ_{E1} imposed. It is surprising that the disk spring with Φ_{E2} imposed produces the load-displacement curve in Fig. 10a which shows the greatest overall force output; however, as previously predicted, the hysteretic force difference is still the lowest of the tested configurations albeit higher than the analytical predictions. The asymmetric test configurations, Φ_{E3} and Φ_{E4}, show the same general trends in Figs. 10a and 2b. However, there is a distinct overlap of their respective load-displacement curves in Fig. 10a; likewise, their overall range spans almost the entire range of the load-displacement data.

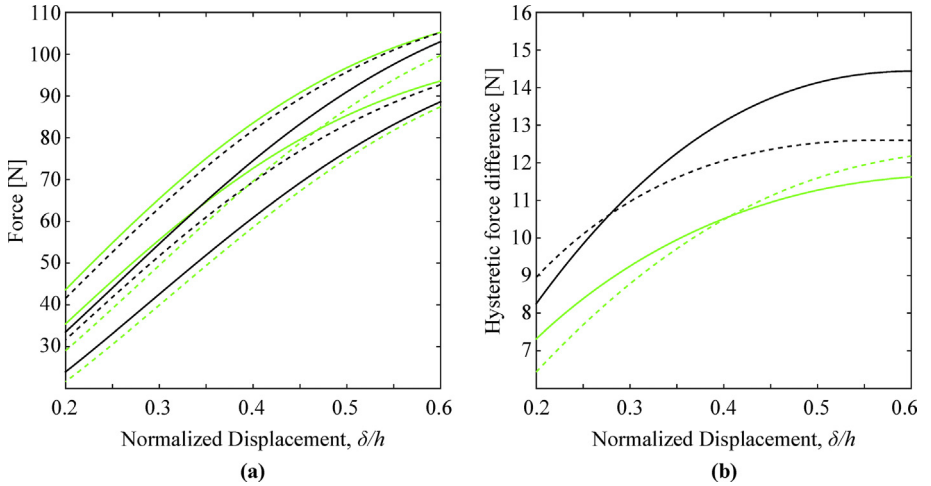

Fig. 10. Measured results using the quasi-static test apparatus (Fig. 3). (a) Load-displacement curves for the four principal experimental fiction conditions (Table 4) and (b) corresponding hysteretic force magnitude for each of the experimental friction conditions. Key: —— Φ_{E1}, —— Φ_{E2}, - - - - Φ_{E3}, and - - - Φ_{E4}.

Table 8
Model designations with parameters.

Model	μ_L	μ_H	c
Υ_1	0.3896	0.4871	c_{L2}
Υ_{1b}	0.3896	0.4871	b
Υ_2	0.3635	0.4553	c_{L2}
Υ_{2b}	0. 3635	0. 4553	b

While the heuristic analysis is useful for discussing general trends, the inconsistent starting point and varying trends in the experimental data makes overlay comparison with theory difficult. Instead, the dissipation energy — the area between the loading and unloading load-deflection characteristic — is selected as a convenient comparison metric between experimental data and analytical results. Then four model configurations of Table 8, based off of Eq. (10), are compared to the experimental results. Table 8 shows the high and low friction coefficients and the value of c for each of the comparison models. Refined models Υ_1 and Υ_{1b} use the experimentally determined friction coefficients from the tilt test (Fig. 4); whereas the friction parameters for models Υ_2 and Υ_{2b} are found by tuning the model such that the dissipated energies for the symmetric friction cases are within 1% of their experimental counterparts.

Using the information from Table 2, c_{L1} and c_{L2} are calculated to be 11.48 mm and 11.43 mm, respectively. For the sake of comparison, the geometric midpoint radius, $(a+b)/2$, is 11.65 mm. It is obvious that the rotation point is nearer to the inner edge regardless of which definition of c is utilized, which means that the friction force at the outer edge will always have a longer moment arm. However, note that the consequence of including material effects in the working assumptions of Curti and Orlando [10] results in the placement of the cross section rotation point closer to the inner edge than the earlier definition of Almen and Laszlo [9]. This implies that the friction at the inner edge would have less influence on the width of the hysteresis than the prior analysis has suggested. Based on heuristic observations of Fig. 10, the asymmetric friction conditions have a much greater impact on the force output than suggested by the theoretical results (Fig. 2). Therefore, c_{L1} has been excluded from that analysis since it is closer to the geometric midpoint radius, which would further diminish the influence of the asymmetric friction conditions. Additionally, models Υ_{1b} and Υ_{2b} examine the extreme limiting case of the cross section rotating about the inner edge contact ($c = b$). While $c = b$ may not be a completely realizable physically, it demonstrates an extreme hypothetical case which could be approached due to the confluence of disk spring geometry, material properties, and boundary conditions at the disk spring edges.

The resulting trends from model Υ_1 (Figs. 11a and 11b) and model Υ_2 (Figs. 11c and 11b) are reasonably representative of the trends observed in the quasi-static measurements displayed in Fig. 10. However, neither model Υ_1 nor model Υ_2, where $c = c_{L2}$, illustrate the district separation between asymmetric friction conditions which was exhibited by the analogous experimental conditions in the load-displacement relationship as well as the hysteretic force difference. As shown in Figs. 11a and 11c, the load-displacement relationship of the asymmetric friction cases overlay each other such that they are almost indistinguishable. Conversely, models Υ_{1b} and Υ_{2b}, where $c = b$, begin to show a separation between the load-displacement relationships of the asymmetric friction cases in Figs. 12a and 12c, respectively. These results are magnified when looking at the hysteretic force difference curves of the asymmetric case. As seen in Figs. 12b and 12d, there is a clear and distinct separation of the hysteretic force difference curves for the asymmetric cases that indeed more closely approx-

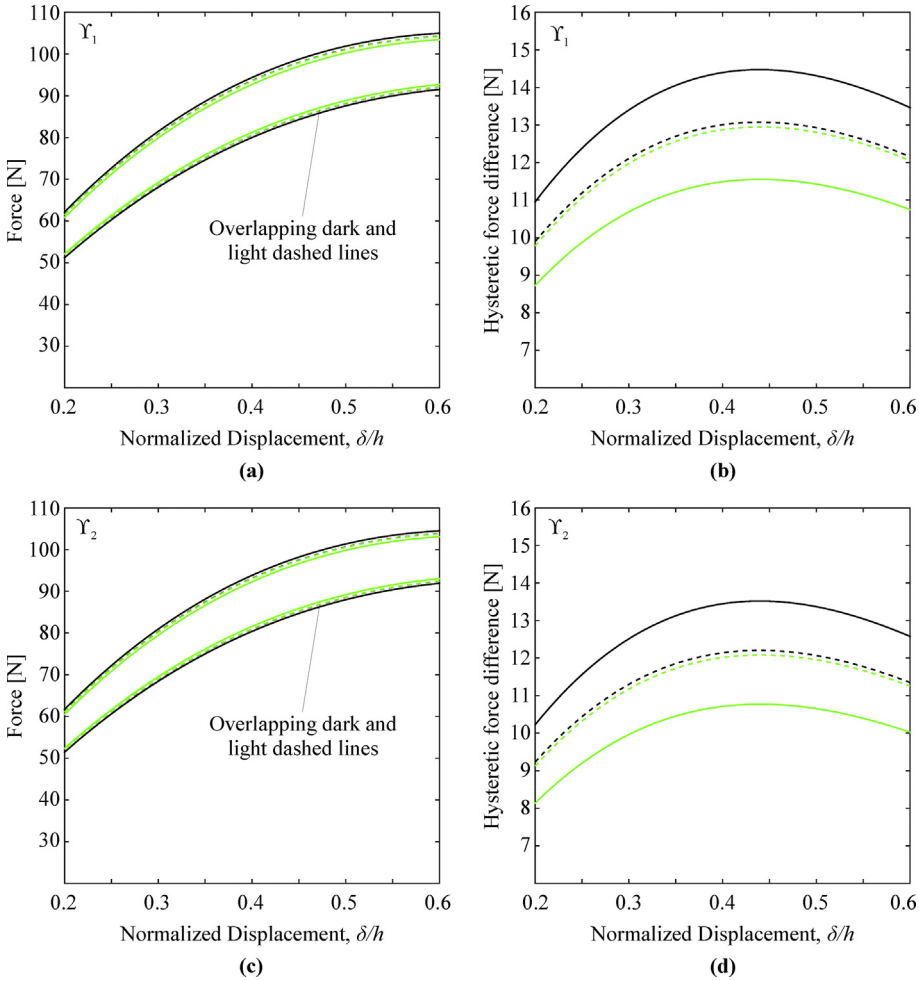

Fig. 11. Analytical results for refined models Υ_1 and Υ_2 ($c = c_{L2}$) for the conditions described in Table 8. (a) Load-displacement curves for model Υ_1, (b) hysteretic force difference curves for model Υ_1, (c) load-displacement curves for model Υ_2, and (d) hysteretic force magnitude curves for model Υ_2. Key: —— Φ_1, —— Φ_2, - - - - Φ_3, and - - - - Φ_4.

imates the difference exhibited by the experimental results. Furthermore, this adds credence to the notion that the prior analytical derivation of the cross section rotation point location may not be entirely accurate; conversely, it could also indicate that the assumptions of the deformation mechanisms must be re-examined.

Due to c having no influence in symmetric friction conditions, it is not surprising that the symmetric cases of models Υ_1 and Υ_{1b} have identical dissipative energies — shown in Table 9. Likewise, models Υ_2 and Υ_{2b} have the same relationship. Symmetric friction cases where the coefficient of friction has been determined via tilt test, models Υ_1 and Υ_{1b}, show a larger deviation from the dissipative energies determined from the experimental results — approximately 6.8% and 7.0% for the high and low symmetric friction cases, respectively, with respect to the experimental results. The coefficients of friction for models Υ_2 and Υ_{2b} have been numerically adjusted such that the dissipative energy differs from experiment by under 1% as stated previously. Using the same level of precision on the coefficients of friction as the tilt test results, the dissipative energies are matched to three decimal places with relative ease. The percent differences of models Υ_1 and Υ_{1b}, with respect to the measurements, range from approximately 6% to 25% for conditions Φ_{E3} and Φ_{E4}. Therefore, it is more prudent to assume that a good agreement with the experimental results would assure that either model Υ_2 or model Υ_{2b} should reasonably predict the dissipative energy of the asymmetric friction conditions. As seen in Table 9, the dissipative energy exhibited by the experiment under condition Φ_{E3} is reasonably well predicted by both models Υ_2 and Υ_{2b} having percent differences of 1.03% and 4.03%, respectively. Conversely, models Υ_2 and Υ_{2b} do not correlate as well with the experiment subjected to Φ_{E4} condition as demonstrated by their respective percent differences — 17.7% and 10.6%. These results suggest that the true value of c is bounded by c_{L2} and b. Furthermore, model Υ_2 having better correlation with results from Φ_{E3} and model Υ_{2b} corresponding better with Φ_{E4} indicates that the value of c is not a geometrically defined parameter as it moves towards whichever edge has the greater friction magnitude. If the location of the rotation point were dictated by geometry

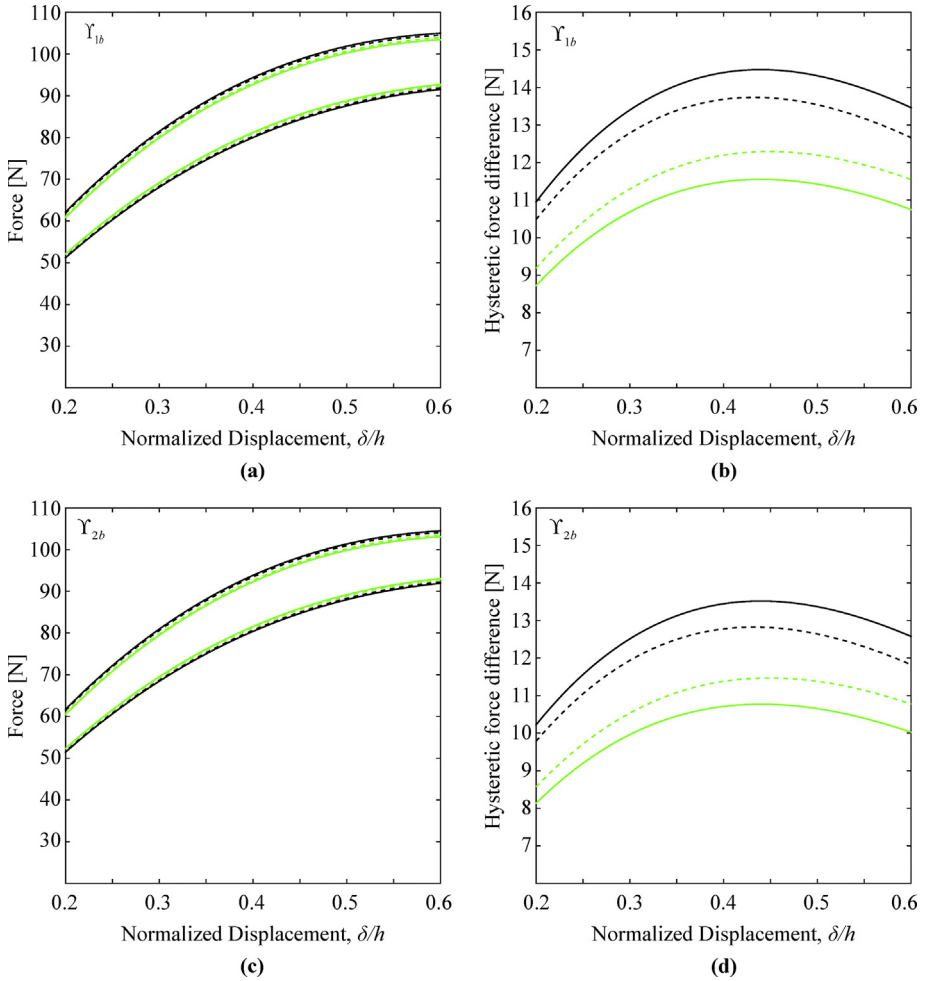

Fig. 12. Analytical results for refined models Υ_{1b} and Υ_{2b} ($c = b$) for the conditions described in Table 8. (a) Load-displacement curves for model Υ_{1b}, (b) hysteretic force difference curves for model Υ_{1b}, (c) load-displacement curves for model Υ_{2b}, and (d) hysteretic force magnitude curves for model Υ_{2b}. Key: —— Φ_1, —— Φ_2, - - - - Φ_3, and - - - Φ_4.

Table 9
Comparison of dissipation energies of hysteresis loop bounded by displacement range of interest for experimental and analytical results – refer to Table 8 for model designations.

	Dissipation energy (mJ)			
Method	Φ_{E1}	Φ_{E2}	Φ_{E3}	Φ_{E4}
Experiment (Fig. 7a)	3.572	2.846	3.258	2.672
Model Υ_1	3.825	3.052	3.456	3.420
Model Υ_{1b}	3.825	3.052	3.633	3.243
Model Υ_2	3.572	2.846	3.225	3.192
Model Υ_{2b}	3.572	2.846	3.392	3.026

alone, differences between the experimental and models should have remained relatively constant for the asymmetric friction cases.

No prior studies specifically examining the stiffness parameters of disk springs are available since the literature [3,4,9–26] has primarily focused on load-deflection characteristics, which is largely due to its current main usage as a preload element. Since the stiffness parameters are vitally important in dynamic analysis, their determination around an operating point (over the midrange of working displacements) is briefly investigated next. For the sake of illustration, the load-deflection characteristics of model Υ_2, model Υ_{2b} (Figs. 11c and 12c, respectively), and the measured load-deflection characteristic (Fig. 10a) are numerically differentiated. Table 10 shows typical stiffness parameters at the deflection midpoint of the disk spring for both analytical and experimental studies. Table 10 shows that there are no perceptible differences between the stiffness parameters of models Υ_2 and Υ_{2b} regardless of which principal friction condition is imposed, nor which process – loading

Table 10
Comparison between theory and measurement based stiffness parameter (N/mm) computations at a midrange deflection point ($\delta/h = 0.4$)—refer to Table 8 for model designations.

	Loading midpoint			Unloading midpoint		
Friction condition	Υ_2	Υ_{2b}	Measurement	Υ_2	Υ_{2b}	Measurement
Φ_1	141.3	141.6	278	137.4	137.2	258
Φ_2	141.3	141.6	249	137.4	137.2	236
Φ_3	141.3	141.6	256	137.4	137.2	246
Φ_4	141.3	141.6	283	137.4	137.2	263

or unloading – is under consideration. Comparing the analytically determined values to measurement shows that the stiffness parameters are of the same order of magnitude; however, the numerical differences between the analytical and experimental stiffness parameters are considerable ranging from approximately 50% to 70%. While the analytical load-deflection characteristics are sufficient for mechanical design, stiffness discrepancies suggest that the proposed model needs further refinements before dynamic and vibration studies are conducted.

9. Conclusion

On a fundamental note, this article overcomes the void in analytical load-deflection formulations for coned disk springs [9,10,12–18,20–23] which have been widely used for a century. First, a refined single disk spring model, capable of having asymmetric friction conditions imposed on the disk spring edges, has been developed to predict the load-deflection and quasi-static hysteresis characteristics; unlike the assumptions made in prior studies, the new formulation allows each of the disk spring contact edge friction conditions to be independently varied. Second, a new quasi-static disk spring characterization experiment (with independently variable contact surfaces) has been successfully developed and carefully validated by comparing analytical and experimental methods for a linear helical spring. Additionally, the limiting cases – equal friction on the inner and outer edges of the disk spring — of the proposed experiment are consistent with results of prior studies [15,16,18,19,21]. Third, new measurements on the coned disks show that there is a significant friction contribution from the edges which does affect the magnitude of hysteresis. Distinct differences in the hysteresis magnitude, as a function of the displacement, are observed between the four experimentally implemented principal friction conditions, which are not quite apparent in the analytical models. Such results from the asymmetric friction conditions suggest that some of the long standing assumptions in disk spring theories [1–4,9–23] may not be applicable in general. The highly nonlinear, load-dependent stiffness and damping characteristics of disk springs have potential to be useful in vibration isolation applications [1,2,5–8,26]. While the proposed load-deflection characteristics are useful in static design methodologies, the large difference observed between theory and measurement based disk spring stiffness parameters (over midrange of working displacements) suggests that further analytical and experimental work is needed from the dynamic isolation perspective [5–8].

Appendix A. List of symbols

a	Mid-surface outer radius
b	Mid-surface inner radius
c	Neutral circle radius
d	Helical spring wire diameter
D	Helical spring mean diameter
E	Young's modulus
h	Cone height
H	Disk spring height
k	Stiffness parameter
ℓ	Linear helical length
M	Moment
N	Number of samples
P	Spring force resultant
s	Standard deviation
SE	Standard error
α	Radii ratio (a/b)
β	Cone base angle
δ	Axial spring deflection
η	Helical spring number of coils

θ	General angle
μ	Static coefficient of friction
ν	Poisson's ratio
τ	Shell thickness
Υ	Comparison model
φ	Relative rotational displace of disk spring cross section
Φ	Friction condition
ψ	Sector angle of disk spring
Subscripts	
0	Initial
a	Outer edge
b	Inner edge
DS	Disk spring
e	Edge
E	Experiment
f	Friction (includes friction)
H	High
HS	Linear helical spring
L	Low
*L*1	Literature – Ref. [9]
*L*2	Literature – Ref. [10]
*L*3	Literature – Ref. [13]
*L*4	Literature – Ref. [18]
P	Manifests due to spring force
*R*1	Reaction due to radial displacement
*R*2	Reaction due to change in curvature
s	Relating to general static friction
TF	Test frame
Superscripts	
$\overline{()}$	Arithmetic mean

References

[1] Schnorr Handbook for Disk Springs, fourteenth ed., Adolf Schnorr GmbH, Sindelfingen, Germany, 1983.
[2] Precision Disc Springs, Century Spring Corp. and MW Industries Inc, Los Angeles, CA, and Baltimore, MD, USA, 2015.
[3] P. Bühl, Maximale Höhen bei Tellerfedern aus Sonderwerkstoffen, DRAHT-Fachz (1972) 63–65.
[4] C.K.H. Dharan, J.A. Bauman, Composite disc springs, Compos. Part Appl. Sci. Manuf. 38 (2007) 2511–2516, http://dx.doi.org/10.1016/j.compositesa.2007.08.008.
[5] D. Muster, R. Plunkett, Isolation of vibrations, in: L.L. Beranek (Ed.), Noise and Vibration Control, revised ed., Inst. Noise Cont. Eng., Washington D.C., USA, 1988, pp. 424–427.
[6] A. Carrella, M.J. Brennan, T.P. Waters, Optimization of a quasi-zero-stiffness isolator, J. Mech. Sci. Tech. 21 (2007) 946–949, http://dx.doi.org/10.1007/BF03027074.
[7] A. Carrella, M.J. Brennan, I. Kovacic, T.P. Waters, On the force transmissibility of a vibration isolator with quasi-zero-stiffness, J. Sound Vib. 322 (2009) 707–717, http://dx.doi.org/10.1016/j.jsv.2008.11.034.
[8] X. Sun, X. Jing, Multi-direction vibration isolation with quasi-zero-stiffness by employing geometrical nonlinearity, Mech. Syst. Signal Process. 62–63 (2015) 149–163, http://dx.doi.org/10.1016/j.ymssp.2015.01.026.
[9] J.O. Almen, A. Laszlo, The uniform-section disk spring, Trans. ASME 58 (1936) 305–313.
[10] G. Curti, M. Orlando, A new calculation of coned annular disk spring, in: Proc. ASME Winter Annual Meet., New York, NY, USA, 76-WA/DE-9, 1976.
[11] G. Curti, M. Orlando, G. Podda, Experimentelle Nachprüfung eines neuen Berechnungsverfahrens für Tellerfedern, DRAHT 31 (1980) 26–29.
[12] G. Curti, M. Orlando, Ein neues Berechnungsverfahren für Tellerfedern, DRAHT 30 (1979) 17–22.
[13] G. Curti, M. Orlando, G. Podda, Vereinfachtes Verfahren zur Berechnung con Tellerfedern, DRAHT 31 (1980) 789–792.
[14] G. Curti, D. Appendino, Vergleich von Berechnungsverfahren für Tellerfedern, DRAHT 33 (1982) 38–40.
[15] K.-H. Muhr, P. Niepage, Über die Reduzierung der Reibung in Tellerfedersäulen, Konstruktion 20 (1968) 414–417.
[16] P. Niepage, Über den Einfluß der Reibung und Kreiskegelförmiger Lasteinleitungselemente auf die Kennlinie von Einzeltellerfedern und Tellerfederpaketen, Konstruktion 36 (1984) 379–384.
[17] G. Curti, R. Montanini, Theoretical, numerical, and experimental analysis of conical disk springs, in: XXV AIAS Natl. Conf. Int. Conf. Mat. Eng., Gallipoli, Lecce, Italy, 1996, pp. 573–581.
[18] G. Curti, R. Montanini, On the influence of friction in the calculation of conical disk springs, Trans. ASME 121 (1999) 622–627, http://dx.doi.org/10.1115/1.2829508.
[19] G. Curti, R. Montanini, G. Barbato, Determinazione sperimentale del coefficiente di attrito in molle a disco conico, in: Atti IV Congr. Naz. Misure Mecc. E Termiche, Dipartimento di Energetica, Università degli Studi di L'Aquila, L'Aquila, Abruzzo, Italy, 1999, pp. 29–40.
[20] M. Boivin, J. Bahuaud, Calccul des ressorts diaphragmes, Mecanique (1974) 24–31.
[21] A.M. Wahl, Mechanical Springs, first ed., Penton Publishing Company, Cleveland, OH, USA, 1944, pp. 238–262.
[22] S. Timoshenko, Strength of Materials Part II: Advanced Theory and Problems, second ed., D. Van Nostrand Co., Inc, Lancaster, PA, USA, 1948, pp. 182–183.
[23] R. Schmidt, G.A. Wempner, The nonlinear conical spring, J. Appl. Mech. 681–682 (1959).

[24] K.-H. Hertzer, Über die Dauerfestigkeit und das Setzen von Tellerfedern, Konstruktion 14 (1962) 147–153.
[25] G. Schremmer, Dynamische Festigkeit von Tellerfedern, Konstruktion 17 (1965) 473–479.
[26] P. Bühl, Mechanische Schwingungen bei Tellerfedersäulen, DRAHT-Fachz (1977) 48–53.
[27] MTS. Elastomer Test Systems. Available: <www.mts.com> (accessed 4 Dec. 2016).
[28] LINK. Model 1620 Compressibility Machine. Available: <www.linkeng.com> (accessed 4 Dec. 2016).
[29] Omega. LVDT Precision DC Gaging Transducers for Quality Control or Automation Tooling. Available: <www.omega.com> (accessed 3 Dec. 2016).
[30] Omegadyne. LCR Series Load Cell. Available: <www.omegadyne.com> (accessed 3 Dec. 2016).
[31] Technical Data: 3M Lapping Film Aluminum Oxide 254X, 261X, 262X, 263X, 265X, 266X, 268X, 264M, Elect. Mark. Mats. Div., 3M Electronics, St. Paul, MN, USA, 2007.
[32] D.T. Greenwood, Advanced Dynamics, Cambridge University Press, New York, NY, USA, 2003, pp. 30–31.
[33] R.C. Juvinall, K.M. Marshek, Fundamentals of Machine Component Design, fourth ed., John Wiley & Sons Inc, Hoboken, NJ, USA, 2005, pp. 470–475.
[34] AZO Materials. (2012 Sept. 21). AISI 1050 Carbon Steel (UNS G10500). Available: <www.azom.com> (accessed 4 Dec. 2016).
[35] AZO Materials. (2012 Sept. 21). AISI 1095 Carbon Steel (UNS G10950). Available: <www.azom.com> (accessed 4 Dec. 2016).